11697

Metal/Oxide Interfacial Reactions: Oxidation of Metals on SrTiO₃ (100) and TiO₂ (110)

Qiang Fu and Thomas Wagner*

Max-Planck-Institut für Metallforschung, Heisenbergstrasse 3, D-70569 Stuttgart, Germany

Received: February 3, 2005; In Final Form: April 14, 2005

We studied chemical reactions between ultrathin metal films (Al, Cr, Fe, Mo) and single-crystal oxides (SrTiO₃ (100), TiO₂ (110)) with X-ray photoelectron spectroscopy (XPS). The work function of the metal and the electron density in the oxide strongly influence the reaction onset temperature (T_{RO}), where metal oxidation is first observed, and the rate of metal oxidation at the metal/oxide interfaces. The Fermi levels of the two contacting phases affect both the space charges formed at the interfaces and the diffusion of ionic defects across the interfaces. These processes, which determine metal oxidation kinetics at relatively low temperatures, can be understood in the framework of the Cabrera–Mott theory. The results suggest that the interfacial reactivity is tunable by modifying the Fermi level (E_F) of both contacting phases. This effect is of great technological importance for a variety of devices with heterophase boundaries.

1. Introduction

Interface formation between metals and oxides is often accompanied by atom and charge exchange across the contacting surfaces. Interfacial chemical reactions will occur in case of mass transport across the interfaces driven by nonequilibrium conditions. Depending on the specific conditions, interdiffusion zones or new phases may form at the interface. As device geometries scale down into the nano regime, interfacial reactivity is a particularly decisive parameter for the performance of the combinations of metals and oxides. For example, metal catalysts supported on oxides generally have dimensions of a few nanometers. The reaction between the metal nanoclusters and the oxide support, often called strong metal–support interaction (SMSI),[1–3] significantly affects catalytic properties. Semiconductor devices are shrinking to smaller and smaller dimensions, e.g., at present down to the sub-0.1 μm range for transistors. The interfaces between the gate oxide and overlying gate electrode and underlying Si channel are dominant factors in determining the device's overall electric properties.[4] Undesirable reactions at the interfaces lead to drastic deterioration of the device's electric properties. Therefore, it is important to understand and control reactions at metal/oxide interfaces and thereby tailor the interfacial reactivity in a well-defined manner.

Thermodynamics is often used to predict chemical reactions. For example, a redox reaction at a metal/oxide (MeⅠ/MeⅡOₓ) interface producing oxidized metal (MeⅠOᵧ) and reduced oxide (MeⅡOᵤ) may be written as follows:

$$Me^I + Me^{II}O_x \rightarrow Me^I O_y + Me^{II}O_{x-y}$$
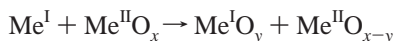
The change in total Gibbs free energy of the reaction (ΔG_R) will tell whether the reaction is possible. Neglecting changes in entropy for solid-state reactions, the standard enthalpy of formation of metal oxides ($\Delta H_f°$)[5] or the oxygen affinity of metals (pO)[6] is widely used for a simple description of the interfacial reactivity.[7–10] However, restrictions of such calculations should be addressed. The thermodynamic data of interfacial

reactants and products involved in the reactions are often unavailable, and bulk thermodynamic data are used for the calculation. These data are frequently different from those of the actual interfacial phases. Second, the chemical composition of the interfacial phases is often unknown. For example, if oxidized metal (MeⅠOᵧ) and reduced oxide (MeⅡOₓ₋ᵧ) possess different stoichiometries, complex phases may form at the interfaces. Accurate phase determination is complicated, since the resulting phases are often approximately a few atomic layers or unit cells thick. Thus, calculations can only be performed assuming specific reaction phases. Moreover, reactions at solid–solid interfaces are often kinetically limited and reaction kinetics must be considered.[9,10]

Interfacial reaction kinetics is generally controlled by mass transport across the phase boundary. The mass transport rate is a function of temperature, atmosphere, dopant concentration, etc.[11,12] For ionic defects, an additional important factor is the presence of space charge layers, which induce an electric field E_0 at the interfaces.[11–13] Such an electrostatic field modifies the activation energy for ionic diffusion at zero electric field from E_a to $E_a \pm qaE_0/2$ (q is ionic defect charge, a is distance between atoms). The additional term describes the additional driving or retarding force for the transport of ionic defects. At relatively low temperatures, $k_BT \ll E_a$ (k_B is the Boltzmann constant, T is the absolute temperature), the diffusion of ionic defects is thermally limited and the space charges modify the activation energy for ionic defect diffusion, which significantly changes the reaction kinetics.

The interplay between interfacial reaction kinetics and space charges has been well investigated for solid–gas reactions, including the oxidation of metals in oxidizing gases and the etching of semiconductor surfaces in fluorine-containing gases.[12–18] These reactions were shown to strongly depend on the space charges originating from charge redistribution at the interfaces and the electronic structure of the metals (work function ϕ_M) or semiconductors (Fermi level E_F). Several well-known theories were developed to describe the reaction processes, such as the Cabrera–Mott theory[13] and the From-hold–Cook theory.[12] We studied reactions at solid–solid interfaces using metal/oxide model systems. In these model

* Corresponding author: E-mail: t.wagner@fkf.mpg.de, Tel. +49-711-689 1429, Fax +49-711-689 1472.

TABLE 1: T_{RO} for Cr Oxidation on Different STO Crystals

STO crystal	pretreatment	T_{RO} (°C)
#1	undoped, strongly reduced	> 810[a]
#2	Nb-doped, UHV heating	760
#3	undoped, UHV heating	640
#4	Fe-doped, UHV heating	460
#5	undoped, oxidized	280

[a] Maximum temperature reached in UHV during this experiment: $T = 810$ °C.

systems, ultrathin metal films or nanosized metal clusters were supported on well-defined single-crystal oxides and subjected to surface and interface analyses by different authors.[8,9,19,20] The reaction kinetics for the solid–solid interfacial reactions was found to be controlled by the space charges at the interfaces and the electronic structure of both solid phases. The basic concept developed for solid–gas reactions[12,13] can be applied to solid–solid reaction processes.

In a preceding paper,[21] encapsulation reactions at metal/oxide interfaces were studied using Pd/TiO$_2$ (110) model systems. A strong dependence of the encapsulation reaction on the electronic structure of both the metal and oxide was observed. In the present paper, we used the model systems metal/SrTiO$_3$ (100) and metal/TiO$_2$ (110) to study oxidation reactions at the solid–solid interfaces. The metal oxidation on oxides was again found to depend on the electronic structure of both phases. Both reactions at the solid–solid interfaces were dominated by the same mechanism as that in solid–gas reactions, which can be understood in the framework of Cabrera–Mott theory. The results indicate that chemical reactions at Me^I/Me^{II}O$_x$ interfaces can be tuned by a distinct variation of the electronic structure in the metals and/or oxides, i.e., a modification of the Fermi levels E_F of the solids.

2. Experimental Section

Interfacial reactions were studied between ultrathin metal films (metal clusters) (Al, Cr, Fe, and Mo) and single-crystal SrTiO$_3$ (STO) (100) and TiO$_2$ (110) substrates. These four metals were selected because they are reactive and possess significantly large differences in oxygen reactivity. STO and TiO$_2$ were chosen because their surfaces and defect chemistries are well studied and can be varied in a well-controlled manner.[21–30]

Preparation of the STO Substrates. Five single-crystal STO (100) substrates (10 mm × 10 mm × 0.5 mm, polished on one side, with a surface miscut of <0.1°) were prepared by different procedures (Table 1). Nb-doped (Nb: donor, 0.2 at. %), undoped, and Fe-doped (Fe: acceptor, 0.14 at. %) STO substrates, designated as #2, #3, and #4, respectively, were treated as follows.[25–27] Etching in buffered HF solution selectively removed the SrO groups on the STO surface, leaving behind a TiO$_2$-termination. Annealing in pure O$_2$ (1 bar) produced straight surface steps and large terraces. Finally, annealing in UHV at 820 °C for 1 h removed surface impurities. The oxygen partial pressure, (pO$_2$), in the UHV chamber is estimated at 10^{-13} bar. In addition, an etched and undoped STO crystal was more strongly reduced by coating the backside with a 2 μm thick Zr film and heating in UHV at 820 °C for 1 h (#1, pO$_2 \cong 10^{-33}$ bar due to the strong reduction by Zr). Another etched, undoped STO crystal was oxidized in pure O$_2$ (pO$_2 =$ 1 bar) at 1100 °C for 1 h, followed by mild Ar$^+$ sputtering (200 eV, 1 min, beam current: 5 mA, #5) to remove surface impurities without influencing the interfacial reactions.[31] This will be discussed later in more detail. The colors of the treated crystals varied from dark blue for #1 to lightly yellow for #5.

Preparation of the TiO$_2$ Substrates.[30] Three different TiO$_2$ (110) crystals were used as substrates: TiO$_2$ A, Nb-doped TiO$_2$ (110) (Nb: donor, 0.01 at. %), Ar$^+$ sputtered (200 eV, 10 min), and UHV annealed at 800 °C for 1 h; TiO$_2$ B, undoped TiO$_2$ (110), Ar$^+$ sputtered (200 eV, 10 min), and UHV annealed at 800 °C for 1 h; TiO$_2$ C, undoped TiO$_2$ (110) heated in air at 800 °C for 6 h and lightly Ar$^+$ sputtered (200 eV, 1 min). Auger electron spectroscopy (AES) and X-ray photoelectron spectroscopy (XPS) after surface treatment failed to detect any impurities on the STO and TiO$_2$ substrate surfaces.

The metal deposition was carried out in a commercial multichamber molecular beam epitaxy (MBE) system (Metal 600, DCA Instruments) with a base pressure of $\sim 5 \times 10^{-9}$ Pa.[27] Ultrathin Al, Cr, Fe, and Mo (purity: 99.99%) films (nominal thickness of 6 Å) were evaporated from effusion cells or electron beam evaporators at room temperature. The residual pressure in the chamber was below 10^{-7} Pa during evaporation. The amount of evaporated material was monitored by a quartz microbalance. The nominal thickness of 6 Å was sufficiently large that XPS core level shifts due to cluster size effects could be ruled out.[32–34] At the same time the thickness of the metal overlayers was small enough to enable photoelectron detection from the metal/oxide interfaces. The metal overlayers were subsequently subjected to stepwise annealing from room temperature to 900 °C in UHV, with temperature steps of around 100 °C. Every annealing temperature was held for 30 min unless otherwise specified. Afterward, the samples were cooled to room temperature in half an hour.

Following each annealing, XPS measurements were performed at room temperature without breaking the vacuum. The measurements were conducted with a Mg Kα X-ray source (E_0 = 1253.6 eV, 400 W) and a double-pass cylindrical mirror analyzer (Perkin-Elmer, 15-255G) at a pass energy of 50 eV. The spectrometer was calibrated to the Cr 2p$_{3/2}$ binding energy of bulk-like Cr (thick metallic films) at 574.4 eV.[35] For all the oxide substrates no significant charging effects were observed during XPS and AES measurements.

3. Results

3.1 Reaction of Cr on STO #3. During our recent investigation of the thermal stability of Cr clusters on undoped STO #3, we found that the reaction of Cr with the underlying oxide depends strongly on temperature and that Cr on STO #3 was not oxidized below 640 °C in UHV.[27] A more detailed understanding of this reaction process can be obtained by studying other effects, such as influences of surface modifications of STO substrates, the thickness of the Cr overlayers, and the annealing time.

Effect of Surface Defects. In a previous paper, we reported results concerning the oxidation of a 6 Å Cr layer on both lightly sputtered STO #3 substrates (Ar$^+$, 200 eV, 4 min) and on nonsputtered STO #3 substrates.[31] It is known that sputtering oxide surfaces with Ar$^+$ ions introduces oxygen vacancies on the surfaces and surface states in the energy gap of the oxides.[22] This affects nucleation, growth, and bonding of metal adatoms on the oxide surfaces.[33,36,37] A similar oxidation behavior for Cr on both sputtered and nonsputtered STO substrates suggested that surface states are not very decisive for the reaction. Similar phenomena observed by Domenichini et al.[37] for the Mo/TiO$_2$ (110) system also suggest a minor influence of substrate surface stoichiometry on the oxidation behavior of Mo on TiO$_2$.

Effect of Thickness of Cr Overlayers. The thickness of the Cr overlayers did not significantly influence such interfacial reactions. Reactions of nominally 1 and 2 Å thick Cr overlayers

Metal/Oxide Interfacial Reactions

*J. Phys. Chem. B, Vol. 109, No. 23, 2005* **11699**
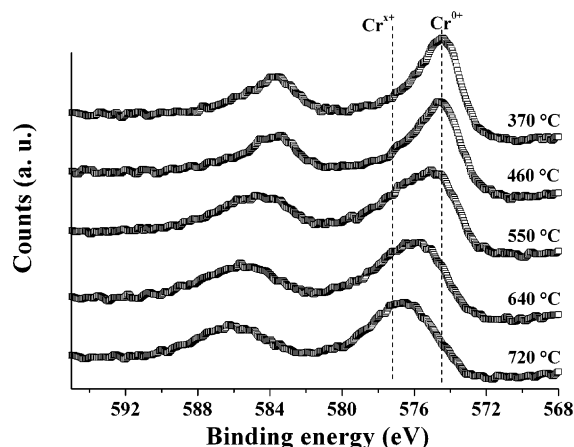
Figure 1. Cr 2p XPS spectra from 2 Å thick Cr layers (nominal thickness, Cr clusters) on STO #3 annealed at different temperatures. Vertical lines label the position of metallic (Cr^{0+}) and oxidized (Cr^{x+}, $x > 0$) Cr.

Figure 2. Cr 2p XPS spectra from 6 Å thick Cr layers (nominal thickness, Cr clusters) on STO #3 annealed at (A) 500 °C and (B) 600 °C for different times. Dotted lines depict the Cr 2p spectrum from metallic Cr (50 nm).

on STO #3 were studied under identical experimental conditions. For example, Figure 1 shows XPS Cr 2p spectra of 2 Å Cr on STO #3 annealed at different temperatures. Cr was found to grow in the form of islands on STO surfaces at room temperature.[27] The smaller nominal thickness (2 Å versus 6 Å) resulted in a smaller Cr cluster size. Spectra recorded from 2 Å Cr overlayers possess a larger full width at half-maximum (fwhm) than that of thicker Cr layers (e.g., 6 Å).[32,33] Consequently, the peak positions rather than the peak shapes of the XPS Cr 2p spectra were used to identify reactions between Cr and STO. The peak positions of the XPS Cr 2p spectra recorded from Cr overlayers heated below 600 °C are quite close to those of bulk Cr except that a small binding energy shift of +0.2 eV originates from cluster size effects.[32−34] A significant change of the peak position was observed above 600 °C. In this case, the binding energy shift is +2 eV, corresponding to the oxidation of the 2 Å thick Cr layer starting at about 600 °C. This behavior is similar to the reaction of a thicker Cr layer (6 Å).[27,31] One would expect that the difference in the nominal thickness of metal overlayers, e.g., 2 Å versus 6 Å, would lead to variations of the cluster size distribution and cluster morphologies. The reactivity of supported metal clusters may vary with their size and shape.[8,9] However, our results suggest that these effects are negligible for Cr oxidation.

Effect of Annealing Time. Figure 2 displays the XPS Cr 2p spectra of Cr overlayers on STO #3 annealed at 500 °C (Figure 2A) and 600 °C (Figure 2B) as a function of time. It was shown that the chemical state of Cr is unchanged at 500 °C, even after an annealing period of 89 h. However, significant shoulder peaks originating from oxidized Cr appear after annealing at 600 °C for several hours. At 700 °C, the 6 Å Cr overlayer was completely oxidized in less than 10 min.[27] These results indicate that the oxidation of Cr on STO is kinetically limited. This can be understood simply by imagining that a temperature difference of about 100 °C typically leads to a change of the reaction rate by a factor of 5 to 10.

The studies detailed above regarding the reactions at the Cr/STO #3 interface indicate that the interfacial reaction is a kinetically limited process. The differences in surface states, cluster sizes, and shapes did not result in a wide variation of the reaction rates. The reactions mainly depend on bulk properties of the metal and the oxide rather than interfacial properties, such as surface states of oxides, cluster size of metals, etc. As shown below, we have applied different systems, including Cr supported on different STO and TiO$_2$ substrates,
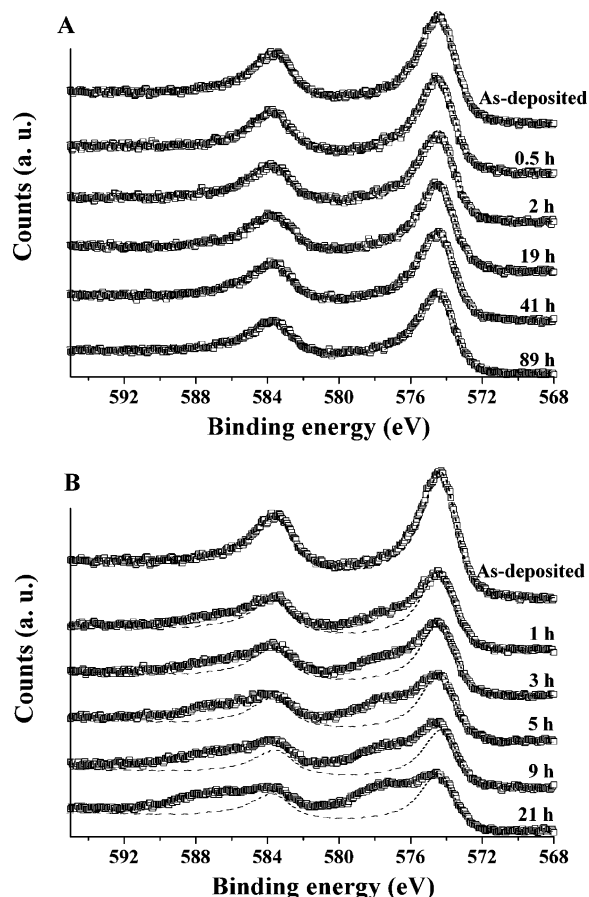
and different metal overlayers deposited on identical oxide crystals. The surface properties of the oxides and the nucleation process of the metals may not be exactly the same. However, the above results enable us to conclude that any large differences in reaction temperature (e.g., > 50 °C) can be attributed to variations of the bulk properties of the contacting phases, which will be discussed in next sections.

3.2 Reactions of Cr on Different STO and TiO$_2$ Crystals. In the following, we will present a systematic investigation of the reactivity of Cr/STO interfaces for the crystals #1 to #5. For comparison, we performed identical experiments for all five Cr/STO systems. A stepwise annealing experiment at elevated temperatures combined with XPS measurements revealed that Cr oxidation depends strongly on the STO substrate pretreatment.

Cr oxidation leads to additional peaks at higher binding energies in the XPS Cr 2p spectra. Line shape changes in the XPS Cr 2p spectra indicate the so-called reaction onset temperature (T_{RO}), where Cr oxidation is first observed. Figure 3 shows selected XPS Cr 2p spectra from five Cr/STO interfaces annealed at different temperatures. To highlight changes from the metallic to the oxidized states, we superimposed the XPS Cr 2p spectrum from a metallic Cr layer (50 nm thick) as dotted line onto the respective spectra. We found that Cr on STO #1 was not oxidized up to 810 °C (T_{RO} > 810 °C) while Cr oxidation occurred on STO #5 below 280 °C. The T_{RO} of Cr oxidation on STO #2, STO #3, and STO #4 were 760, 640, and 460 °C, respectively (see Table 1). The huge difference of
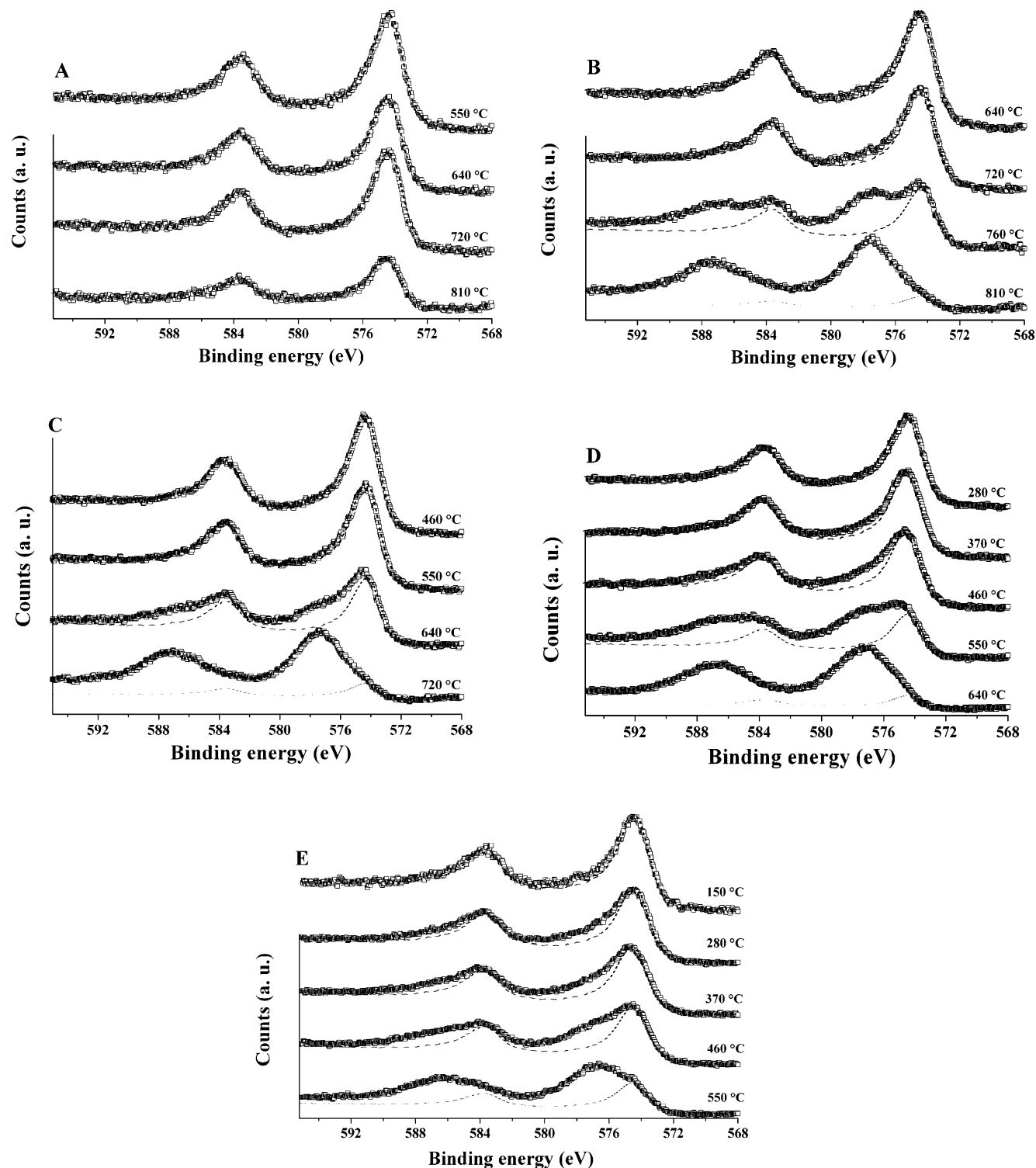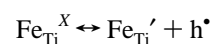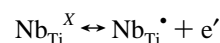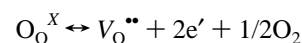
Figure 3. Cr 2p XPS spectra from 6 Å thick Cr layers (nominal thickness, Cr clusters) on differently treated STO crystals: (A) Cr on STO #1; Cr was not oxidized at temperatures ranging up to 810 °C (T_{RO} > 810 °C). (B) Cr on STO #2; T_{RO} = 760 °C. (C) Cr on STO #3; T_{RO} = 640 °C. (D) Cr on STO #4; T_{RO} = 460 °C. (E) Cr on STO #5; T_{RO} = 280 °C.
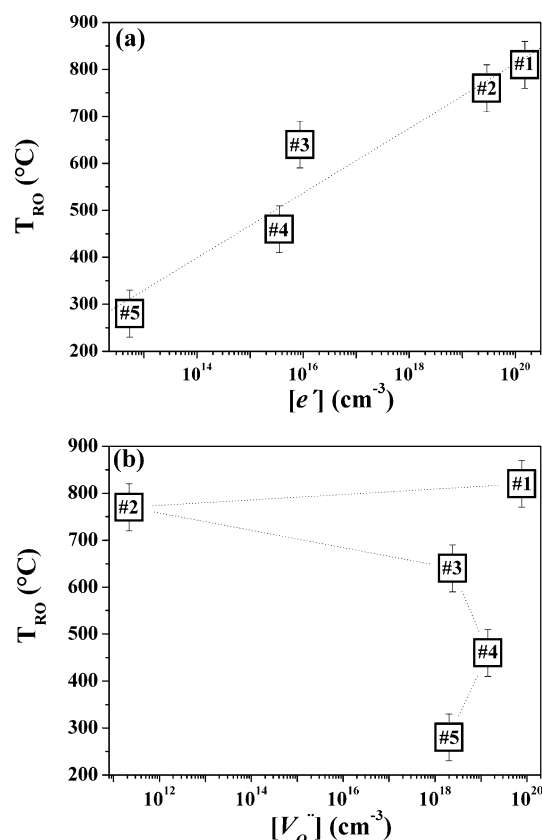
T_{RO} originates from significant variations in the Cr oxidation rates on STO, which decreases in the order Cr/STO #5 to Cr/STO #1.

STO is a mixed conductor prototype whose defect chemistry was extensively studied. Defects mainly include intrinsic ionic defects, such as (Kröger–Vink notation) oxygen vacancies $V_O^{\bullet\bullet}$, strontium vacancies V_{Sr}'', and electronic defects (free carriers: electrons e′ and holes h•). Defect concentration is a function of temperature, pO_2, concentration of extrinsic dopants, etc.[23,24,38]

For example, the following defect equilibria may exist in the solid:

$$O_O^X \leftrightarrow V_O^{\bullet\bullet} + 2e' + 1/2O_2$$

$$Nb_{Ti}^X \leftrightarrow Nb_{Ti}^{\bullet} + e'$$

$$Fe_{Ti}^X \leftrightarrow Fe_{Ti}' + h^{\bullet}$$

Qualitatively, annealing in an oxygen-deficient atmosphere

Metal/Oxide Interfacial Reactions

J. Phys. Chem. B, Vol. 109, No. 23, 2005 **11701**

Figure 4. T_{RO} for Cr oxidation on STO as a function of (a): [e′] and as a function of (b): [$V_O^{\bullet\bullet}$] in the STO crystals #1 to #5.

(e.g., UHV) increases $V_O^{\bullet\bullet}$ and e′ concentrations ([$V_O^{\bullet\bullet}$] and [e′]), while heating in oxygen-rich environment decreases these defect concentrations. Doping the materials with donors, such as Nb and La, reduces [$V_O^{\bullet\bullet}$] and increases [e′], while acceptor doping, such as Fe or Mn, increases both [$V_O^{\bullet\bullet}$] and hole concentration ([h•]).[23,38]

Quantitatively, [e′], [h•], and [$V_O^{\bullet\bullet}$] can be calculated for the differently treated STO crystals using a defect model given by Moos et al.[23] Sr vacancies were assumed to be frozen-in at a concentration of 2.4×10^{18} cm^{-3} for all STO crystals at $T <$ 1200 °C.[24] The oxygen exchange reactions at STO surfaces were regarded to be thermally limited at temperatures below 800 °C, resulting in a fixed [$V_O^{\bullet\bullet}$] at lower temperatures. The defect concentrations were calculated under the corresponding doping and pO_2 conditions at $T = 1100$ K. The electron concentration [e′] or electron density n in the five crystals decreased in the order #1 to #5, while [$V_O^{\bullet\bullet}$] decreased in the sequence #1, #4, #3, #5, #2. The decrease in [e′] was indirectly confirmed by the gradual change of the crystals' color from deep blue (#1) to light yellow (#5). The intensity of the blue color serves as an optical indicator of [e′].[24] Plotting the data of T_{RO} with the [e′] in the corresponding STO crystal reveals a systematic increase of T_{RO} with the [e′] (Figure 4a). A smaller [e′] in STO corresponds to faster oxidation of Cr on STO. However, we did not find such a systematic dependence between T_{RO} and [$V_O^{\bullet\bullet}$] (Figure 4b).

The effect of the electronic structure of TiO$_2$ (110) crystals on Cr oxidation was studied under identical experimental conditions as those in the case of STO. Cr 2p spectra of 6 Å Cr overlayers on different TiO$_2$ (110) crystals (named as A, B, and C) annealed at different temperatures are shown in Figure 5. Cr on TiO$_2$ A started oxidizing at 370 °C, but metallic Cr was still observed at 550 °C (Figure 5A). Cr was almost fully
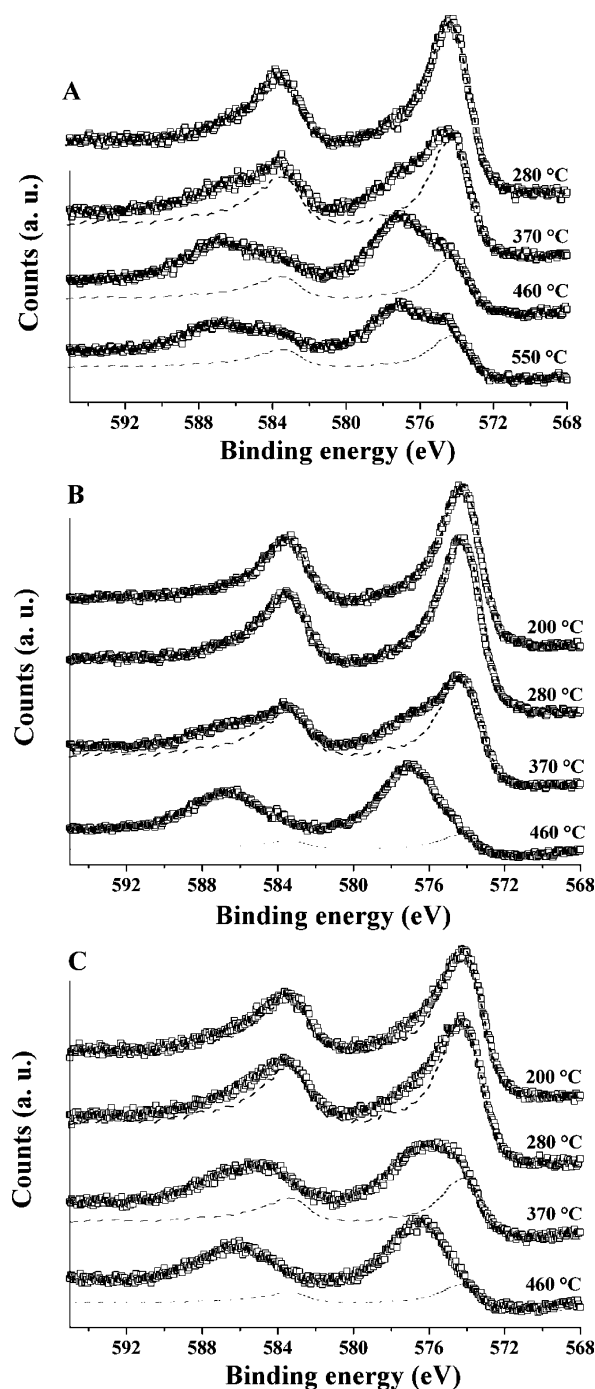
Figure 5. Cr 2p XPS spectra from 6 Å thick Cr layers (nominal thickness, Cr clusters) on differently treated TiO$_2$ crystals: (A) Cr on TiO$_2$ A. (B) Cr on TiO$_2$ B. (C) Cr on TiO$_2$ C. Dotted lines depict the Cr 2p spectrum from metallic Cr (50 nm).

oxidized on TiO$_2$ B at 460 °C (Figure 5B). Figure 5C shows that Cr was lightly oxidized at 280 °C on TiO$_2$ C and nearly converted to Cr oxide at 370 °C.

Considering the defect chemistry of TiO$_2$,[21,28−30] one can conclude that the electron density in Nb-doped crystal (TiO$_2$ A) is higher than that in the undoped substrate (TiO$_2$ B), since Nb is an n-type dopant. The oxidized TiO$_2$ (TiO$_2$ C) possesses an even lower electron density since annealing in an oxygen-rich atmosphere removed oxygen vacancies, the intrinsic donors, in the crystal. The electron density in TiO$_2$ decreases from A to C. These results indicate again that the Cr oxidation rate on TiO$_2$ is inversely proportional to the [e′] in the TiO$_2$. This
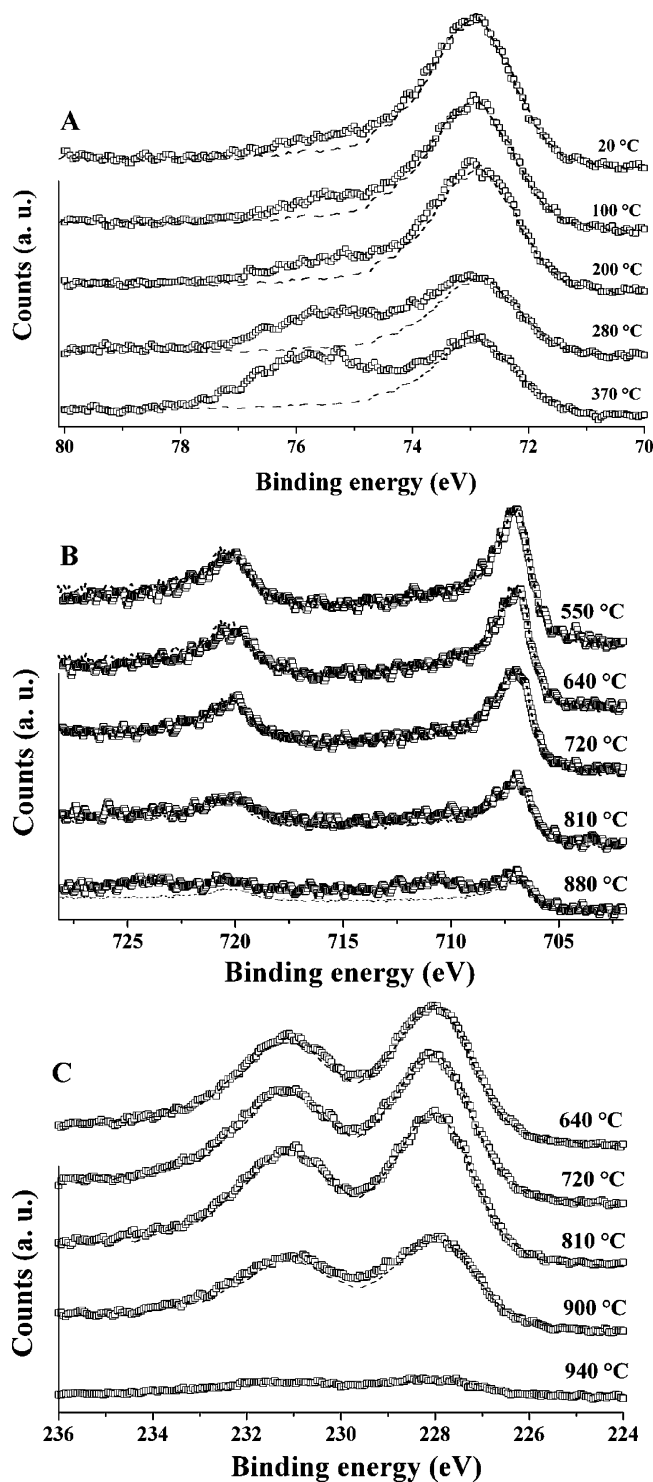
Figure 6. XPS spectra from 6 Å thick metal films (nominal thickness): (A) Al 2p spectra from Al/STO #3, $T_{RO} < 20$ °C. (B) Fe 2p XPS spectra Fe/STO #3, $T_{RO} = 810$ °C. (C) Mo 3d XPS spectra from Mo/STO #3, $T_{RO} = 900$ °C.

behavior is the same as the result of the interfacial reactions in the Cr/STO system (see Figure 4a).

3.3 Reactions of Different Metals on Identical Oxides. To study the effect of metals on the reactions, we have investigated reactions of different metal films (Al, Cr, Fe, and Mo, 6 Å nominal thickness) on identical STO #3 and TiO₂ A substrates. The preparation of the metal/oxide interfaces and annealing experiments of the interfaces are identical to those described in the preceding section. Again, XPS was applied to monitor the interfacial reactions. The oxidation of Al, Cr, and Fe on STO

and TiO₂ causes additional peaks at higher binding energies in the Al 2p, Cr 2p, and Fe 2p spectra. Thus, the T_{RO} of Al, Cr, and Fe on STO and TiO₂ can be similarly determined by monitoring the line shape of the spectra. At the Mo/STO and Mo/TiO₂ interfaces, the oxidation is simultaneously accompanied by desorption of volatile Mo oxides (e.g., MoO₃). Therefore, the line intensity instead of the line shape of the Mo 3d spectra was used to obtain T_{RO}. Sets of the Al 2p, Fe 2p, and Mo 3d spectra from the metal/STO interfaces annealed at different temperatures are given in Figure 6. Al 2p, Fe 2p, and Mo 3d spectra from the metal/TiO₂ interfaces annealed at different temperatures are shown in Figure 7. For comparison, the Al 2p, Fe 2p, and Mo 3d spectra (dotted lines) from the corresponding metallic films were superimposed onto these spectra. T_{RO} for oxidizing four metals on STO and TiO₂ surfaces, obtained from Figures 3c, 5a, 6, and 7, are listed in Table 2.

The electronic structure of the metal films can be characterized by the ϕ_M of the metal surfaces.[5] Al (100), Cr (100), and Fe (100) were epitaxially grown on STO (100) and TiO₂ (110);[30,39] Mo (110) was epitaxially grown on STO (100)[40] and TiO₂ (110).[41] T_{RO} increased with increasing ϕ_M for all metals (Figure 8). The oxygen affinity pO was frequently used to compare the reactivity of metals on oxides. Al and Cr have high pO (pO (Al) = 47.2, pO (Cr) = 32.6),[6] which is consistent with their high reactivity. However, given the similar pO values for Fe and Mo (pO (Fe) = 20.6, pO (Mo) = 20.1),[6] one would expect similar T_{RO} values for the two metals (see Table 2).

4. Discussion

4.1 Role of Space Charges in the Oxidation Reactions. The oxidation of reactive metals on STO or TiO₂ substrates, which requires O^{2-} transport from the oxide bulk to the interface or equivalently an inward diffusion of $V_O^{\bullet\bullet}$ from the interface to the bulk, is driven by an electrochemical potential gradient of $V_O^{\bullet\bullet}$.[8,27] If the rate of oxygen transport across the interface is controlled by $[V_O^{\bullet\bullet}]$, then we would expect a systematic reaction dependence on $[V_O^{\bullet\bullet}]$ in the STO crystals or $[V_O^{\bullet\bullet}]$ in the metal overlayers determined by metal's oxygen affinity. However, such correlations between T_{RO} and $[V_O^{\bullet\bullet}]$ or pO were not observed (see Figure 4b and Table 2). In contrast, the reactions show systematic dependences on $[e']$ in oxides and ϕ_M of the metal films, i.e., E_F in both contacting phases (see Figure 4a and Figure 8).

These results suggest that oxidation was controlled by space charges formed in STO or TiO₂ near the interface. Since the space charges form when the metal and oxide establish contact and the Fermi levels equilibrate, they are a function of the relative E_F position in both phases. In the following, two cases will be discussed: Case (1) E_F of the metal is higher than E_F of the oxide, $E_F (Me^I) > E_F (Me^{II}O_x)$, and Case (2) E_F of the metals is lower than E_F of the oxides, $E_F (Me^I) < E_F (Me^{II}O_x)$. For Case 1, the alignment of E_F induces charge transfer from the metal to the oxide. This will lead to the formation of negative space charges in the oxide. Since the resulting built-in electric field decreases the activation energy for O^{2-} diffusion, it promotes oxygen anion diffusion from the oxide bulk toward the surface. This is schematically shown in Figure 9A. Case 1 favors the onset of interfacial reactions at lower temperatures, for example, in the systems of Cr/STO #5, Al/STO #3, and Al/TiO₂ A. Case 2 results in electron transfer from the oxide into the metal, which builds up positive space charges in the oxide (Figure 9B). The electrostatic field formed at the interface hinders oxygen anion diffusion toward the interface. Thus, Case 2 leads to a tremendous increase in T_{RO}, as observed for Cr/STO #1, Mo/STO #3, and Mo/TiO₂ A.
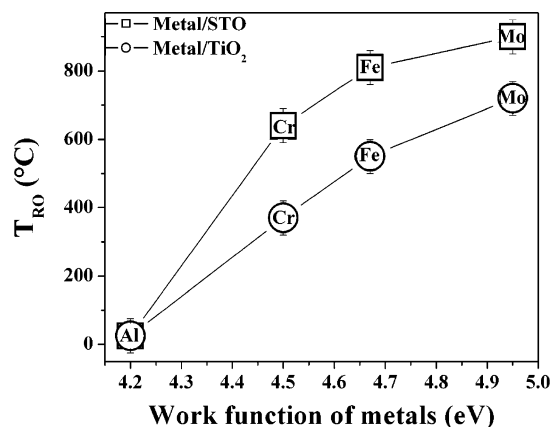
Metal/Oxide Interfacial Reactions

J. Phys. Chem. B, Vol. 109, No. 23, 2005 **11703**
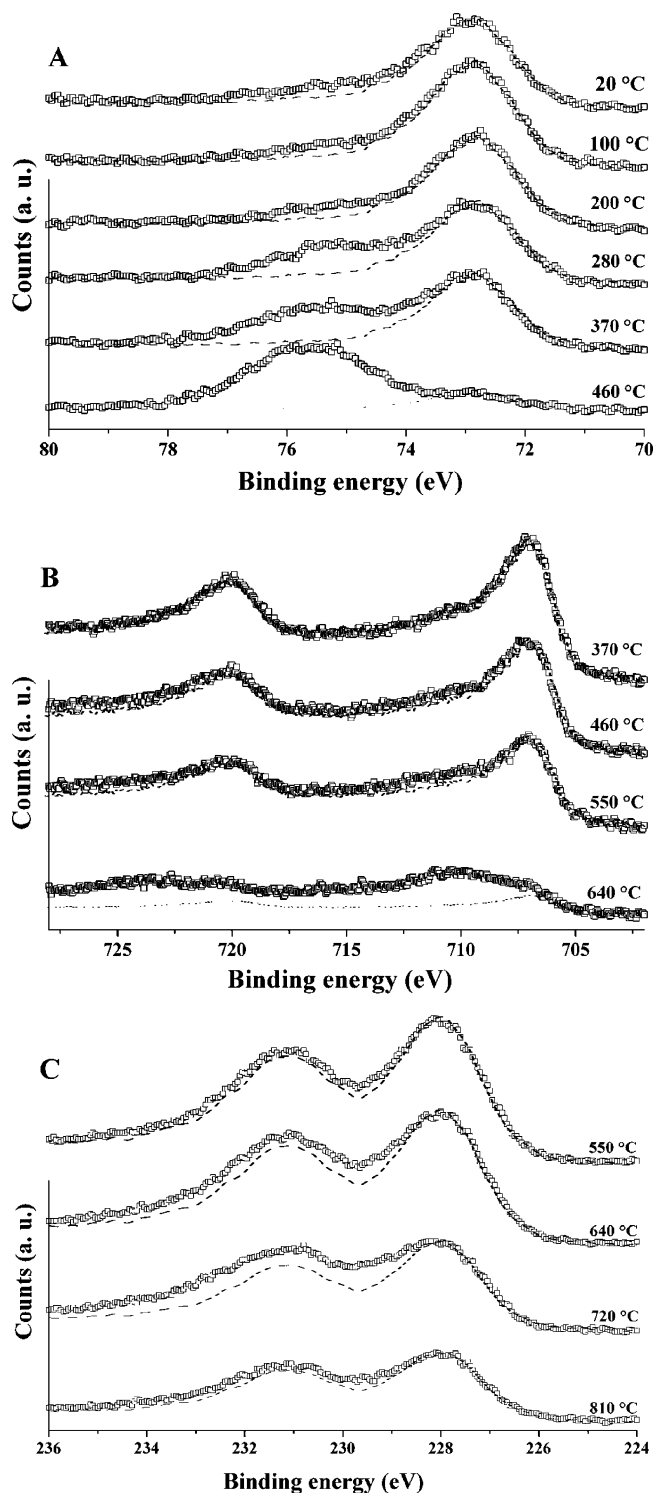
Figure 7. XPS spectra from 6 Å thick metal films (nominal thickness): (A) Al 2p spectra from Al/TiO$_2$ A, T_{RO} < 20 °C. (B) Fe 2p XPS spectra from Fe/TiO$_2$ A, T_{RO} = 810 °C. (C) Mo 3d XPS spectra from Mo/TiO$_2$ A, T_{RO} = 900 °C.

TABLE 2: T_{RO} for the Oxidation of Different Metals on Identical STO #3 and TiO$_2$ A Crystals; ϕ_M is the Work Function of the Metals, and pO is the Metals' Oxygen Affinity

metal films	pO	ϕ_M (eV)	T_{RO} on STO (°C)	T_{RO} on TiO$_2$ (°C)
Al (100)	47.2	4.2	< 20[a]	< 20[a]
Cr (100)	32.6	4.5	640	370
Fe (100)	20.6	4.67	810	550
Mo (110)	20.1	4.95	900	720

[a] Minimum temperature reached in UHV chamber: T = 20 °C.

Figure 8. Plot of T_{RO} (Al, Cr, Fe, and Mo metal films on identical STO #3 and TiO$_2$ A substrates) as a function of ϕ_M.

As discussed in section 3.2, Cr oxidation rate on the five STO crystals increased from #1 to #5 as the electron density decreased. The variation in [e′] results in a shift of E_F from conduction band to the valence band of STO. E_F (Cr) is less than E_F (STO #1),[31] which retards O^{2-} diffusion toward the interface and thereby decreases interfacial reactivity (Figure 9B). As the electron density in the STO decreases, the metal and oxide Fermi levels tend toward each other, and the force retarding O^{2-} diffusion toward the interface weakens. This leads

to a higher interfacial reactivity (from Cr/STO #1 to Cr/STO #4). For Cr/ STO #5, in which E_F (Cr) > E_F (STO),[31] the enhance O^{2-} diffusion toward the interface significantly increases the interfacial reactivity (Figure 9A). The same argument can be applied to explain the dependence of Cr oxidation rates as a function of [e′] in TiO$_2$.

Similar effects are observed by changing the metal from Al to Mo. Since the Al work function is small, E_F (Al) > E_F (STO #3). This promotes O^{2-} diffusion to the interface (Figure 9A) and Al oxidizes at lower temperatures (<20 °C). However, the large work function of Mo may lead to E_F (Mo) < E_F (STO #3) and therefore to low interfacial reactivity.

In summary, a shift of E_F in the oxide relative to that of the metal leads to variations in space charges and built-in interfacial electrostatic fields. This controls the diffusion of O^{2-} ions toward and across the interface and therefore the corresponding interfacial reactivity and oxidation rates.

4.2 General Trends in Interfacial Reactions. We also studied the encapsulation reaction or SMSI at Me^I/Me^{II}O$_x$ interfaces, which showed that the encapsulation reaction is favored by metals with large ϕ_M in contact with n-type doped oxides.[21] If E_F (Me^I) ≪ E_F (Me^{II}O$_x$), then positive space charges form in TiO$_2$ and interstitial titanium cations (Ti$_i^{n+}$, n > 1) diffuse toward the interface. This favors the formation of a suboxide titania layer atop the metal nanoclusters.

A very similar mechanism is also active in solid−gas reactions. The low-temperature oxidation of metal surfaces under oxidizing gases is controlled by the contact potential originating from the energy difference between E_F of the metal and the electronic energy level of the oxidant (so-called "Mott potential" in the Cabrera−Mott theory). This contact potential induces a strong electric field in the oxide film formed, which enables O^{2-} or interstitial metal cation M$_i^{n+}$ diffusion through the oxide scale, even in cases where the thermal activation is quite low. This theory results in a logarithmic law for metal oxidation.[12,13]

Si etching in fluorine-containing gases also relies on a very similar mechanism. It was demonstrated that the surface etching

TABLE 3: Summary of Reactions at Solid−Solid and Solid−Gas Interfaces

interfacial reactions	contacting phases A ‖ B	diffusing species and direction	E_F arrangements favoring reactions
oxidation	metal ‖ oxide	O^{2-}, B → A	E_F (A) > E_F (B)
encapsulation	metal ‖ oxide	Ti_i^{n+}, B → A	E_F (A) < E_F (B)
surface oxidation	metal ‖ gas	O^{2-}, B → A or M_i^{n+}, A → B	E_F (A) > E_F (B)
surface etching	gas ‖ Si	F^-, A → B	E_F (A) < E_F (B)

rates depend strongly on the Si doping: heavily n-doped (n^+) Si etches much faster than undoped Si and lightly n- or p-doped Si, whereas heavily p-doped (p^+) Si exhibits the lowest etching rate.[16,17] The correlation between etching rate and E_F in Si was also explained in the framework of the Cabrera−Mott theory through the interplay between the diffusion of F^- ions into the Si subsurface and surface charges formed at the Si surface.[16,17]

A summary of the four reactions, i.e., oxidation of metals, metal encapsulation, oxidation of metal surfaces in gases, and Si etching, is given in Table 3. In four cases, the interfacial reaction rates are dependent on E_F of the contacting phases. The diffusion of ionic species across interfaces depends on the space charges at the interfaces. Thus, interfacial electronic structure has a strong influence on the reaction kinetics. The Cabrera−Mott theory, which was widely used to describe interfacial reactions at solid−gas interfaces, can be applied to explain both solid−gas and solid−solid interfacial reactions.

Fermi level variations between the contacting phases are directly related to the electric fields generated at the interfaces. A semiquantitative measure of the built-in electric field strength can be obtained by calculating the surface electric field

Figure 9. (A) Negative space charges formed in oxides in the case of E_F (Me^I) > E_F ($Me^{II}O_x$), promoting the outward diffusion of O^{2-}. (B) Positive space charges formed in oxides in the case of E_F (Me^I) < E_F ($Me^{II}O_x$), hindering the outward diffusion of O^{2-}.

magnitude, E_S, i.e., the electric field at the $Me^I/Me^{II}O_x$ interfaces.[31,42,43]

$$E_S = \pm\left(\frac{kT}{qL_D}\right)F(\phi_s,\phi_b)$$

$$F(\phi_s,\phi_b) = \sqrt{2}\left[\sinh\frac{q\phi_b}{kT}\left(\frac{q\phi_b}{kT} - \frac{q\phi_s}{kT}\right) - \left(\cosh\frac{q\phi_b}{kT} - \cosh\frac{q\phi_s}{kT}\right)\right]^{1/2}$$

(+ for ϕ_s > ϕ_b, − for ϕ_s < ϕ_b). ϕ_b is the energy difference between E_F and E_i (intrinsic energy level) of the semiconductor phase (e.g., STO, TiO_2), and ϕ_s is the energy difference between E_F of the metal and E_i of the semiconductor phase. The built-in electric field, E_S, at the interface shows monotonic variations with ϕ_b and ϕ_s. Thus, the interfacial electric field exhibits a systematic dependence on E_F of the metal and oxide. At relatively low temperatures, E_S is a critical parameter that describes transport processes at interfaces (surfaces), including the onset of metal oxidation at metal/oxide interfaces, the encapsulation of metal nanoclusters on oxide, and the reactions on metals or Si surfaces. The systematic dependence of these interfacial reactions on E_F of metals and/or semiconductors and/or oxides is consistent with the monotonic change of E_S with E_F of the contacting phases.[31]

5. Conclusion

We have shown that the reaction kinetics of metal oxidation at metal/STO and metal/TiO_2 (110) interfaces systematically depend on the Fermi levels of both the metal and oxide and that $Me^I/Me_x^{II}O_y$ interfacial reactivity can be tuned by controlling the relative Fermi levels. In many cases this can be done simply via doping, application of external electric fields, illumination of the oxide, or alloying. Our results for metal/oxide interfacial reactions are consistent with the well-known Cabrera−Mott theory and demonstrate that this theory can be extended to include reactions at solid−solid interfaces.

References and Notes

(1) Tauster, S. J.; Fung, S. C.; Garten, R. L. *J. Am. Chem. Soc.* **1978**, *100*, 170.
(2) Haller, G. L.; Resasco, D. E. *Adv. Catal.* **1989**, *36*, 173.
(3) Bell, A. T. *Science* **2003**, *299*, 1688.
(4) Wilk, G. D.; Wallace, R. M.; Anthony, J. M. *J. Appl. Phys.* **2001**, *89*, 5243.
(5) *CRC Handbook of Chemistry and Physics*, 63rd ed.; Weast, R. C., Astle, M. J., Eds.; CRC Press: Boca Raton, 1982.
(6) Reed, T. B. *Free Energy of Formation of Binary Compounds*; MIT Press: Cambridge, 1971.
(7) Lad, R. J. *Surf. Rev. Lett.* **1995**, *2*, 109.
(8) Diebold, U.; Pan, P. M.; Madey, T. E. *Surf. Sci.* **1995**, *331−333*, 845.
(9) Campbell, C. T. *Surf. Sci. Rep.* **1997**, *27*, 1.
(10) Howe, J. M. *Int. Mater. Rev.* **1993**, *38*, 233.
(11) Maier, J. *Prog. Solid State Chem.* **1995**, *23*, 171.
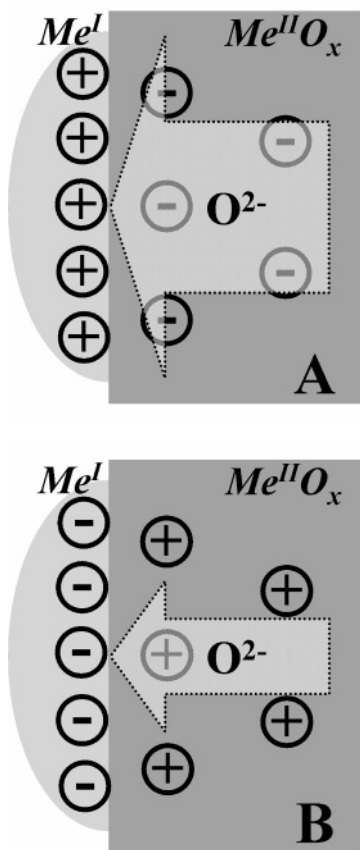
(12) Fromhold, A. T., Jr. *Theory of Metal Oxidation Volume 1 Fundamentals*, North-Holland: Amsterdam, 1976.

(13) Cabrera, N.; Mott, N. F. *Rep. Prog. Phys.* **1949**, *12*, 163.

(14) Roosendaal, S. J.; Vredenberg, A. M.; Habraken, F. H. P. M. *Phys. Rev. Lett.* **2000**, *84*, 3366.

(15) Popova, I.; Zhukov, V.; Yates, J. T., Jr. *Phys. Rev. Lett.* **2002**, *89*, 276101.

(16) Winters, H. F.; Haarer, D. *Phys. Rev. B* **1987**, *36*, 6613.

(17) Van de Walle, C. G.; McFeely, F. R.; Pantelides, S. T. *Phys. Rev. Lett.* **1988**, *61*, 1867.

(18) Qiu, S. R.; Lai, H. F.; Yarmoff, J. A. *Phys. Rev. Lett.* **2000**, *85*, 1492.

(19) Freund H. J. *Surf. Sci.* **2002**, *500*, 271.

(20) Valden, M.; Lai, X.; Goodman, D. W. *Science* **1998**, *281*, 1647.

(21) Fu, Q.; Wagner, T.; Olliges, S.; Carstanjen, H.-D. *J. Phys. Chem. B* **2005**, *109*, 944.

(22) Henrich, V. E.; Dresselhaus, G.; Zeiger, H. J. *Phys. Rev. B* **1978**, *17*, 4908.

(23) Moos, R.; Hrdtl, K. H. *J. Am. Ceram. Soc.* **1997**, *80*, 2549.

(24) Meyer, R.; Waser, R.; Helmbold, J.; Borchardt, G. *J. Electroceram.* **2002**, *9*, 101.

(25) Kawasaki, M.; Takahashi, K.; Maeda, T.; Tsuchiya, R.; Shinohara, M.; Ishiyama, O.; Yonezawa, T.; Yoshimoto, M.; Koinuma, H. *Science* **1994**, *266*, 1540.

(26) Polli, A. D.; Wagner, T.; Rühle, M. *Surf. Sci.* **1999**, *429*, 237.

(27) Fu, Q.; Wagner, T. *Surf. Sci.* **2002**, *505*, 39. Fu, Q.; Wagner, T. *Thin Solid Films* **2002**, *420−421*, 455.

(28) Sasaki, J.; Peterson, N. L.; Hoshino, K. *J. Phys. Chem. Solids* **1985**, *46*, 1267.

(29) Henderson, M. A. *Surf. Sci.* **1999**, *419*, 174.

(30) Diebold, U. *Surf. Sci. Rep.* **2003**, *48*, 53.

(31) Fu, Q.; Wagner, T. *Surf. Sci. Lett.* **2005**, *574*, L29.

(32) Bagus, P. S.; Illas, F.; Pacchioni, G.; Parmigiani, F. *J. Elec. Spec. Relat. Phenom.* **1999**, *100*, 215.

(33) Luo, K.; Clair, T. P.; Lai, X.; Goodman, D. W. *J. Phys. Chem. B* **2000**, *104*, 3050.

(34) Fu, Q.; Wagner, T., unpublished result.

(35) Moulder, J.; Stickle, W. F.; Sobol, P. E.; Bomben, K. D. *The Handbook of the X-ray Photoelectron Spectroscopy*, Pekin-Elmer Corporation, 1992.

(36) Mostfa-Sba, H.; Domenichini, B.; Bourgeois, S. *Surf. Sci.* **1999**, *437*, 107.

(37) Domenichini, B.; Flank, A. M.; Lagarde, P.; Bourgeois, S. *Surf. Sci.* **2004**, *560*, 63.

(38) Smyth, D. M. *Solid State Ionics* **2000**, *129*, 5.

(39) Wagner, T.; Polli, A. D.; Richter, G.; Stanzick, H. *Z. Metallkd.* **2001**, *92*, 701.

(40) Fu, Q.; Tchernychova, E.; Wagner, T. *Surf. Sci. Lett.* **2003**, *538*, L511.

(41) Blondeau-Patissier, V.; Lian, G. D.; Domenichini, B.; Steinbrunn, A.; Bourgeois, S.; Dickey, E. C. *Surf. Sci.* **2002**, *506*, 119.

(42) Kingston, R. H.; Neustadter, S. F. *J. Appl. Phys.* **1955**, *26*, 718.

(43) Sze, S. M. *Physics of Semiconductor Devices*; John Wiley & Sons: New York, 1981.